

**Boundary-Obstructed Topological High- $T_c$  Superconductivity in Iron Pnictides**Xianxin Wu,<sup>1,2,\*</sup> Wladimir A. Benalcazar,<sup>1</sup> Yinxiang Li,<sup>3</sup> Ronny Thomale<sup>Ⓞ</sup>,<sup>4</sup> Chao-Xing Liu,<sup>1,†</sup> and Jiangping Hu<sup>2,5,‡</sup><sup>1</sup>*Department of Physics, Pennsylvania State University, University Park, Pennsylvania 16802, USA*<sup>2</sup>*Beijing National Laboratory for Condensed Matter Physics, and Institute of Physics, Chinese Academy of Sciences, Beijing 100190, China*<sup>3</sup>*Tin Ka-Ping College of Science, University of Shanghai for Science and Technology, Shanghai, 200093, China*<sup>4</sup>*Institut für Theoretische Physik und Astrophysik, Julius-Maximilians-Universität Würzburg, 97074 Würzburg, Germany*<sup>5</sup>*CAS Center of Excellence in Topological Quantum Computation and Kavli Institute of Theoretical Sciences, University of Chinese Academy of Sciences, Beijing 100190, China* (Received 9 April 2020; revised 16 July 2020; accepted 24 August 2020; published 20 October 2020)

Nontrivial topology and unconventional pairing are two central guiding principles in the contemporary search for and analysis of superconducting materials and heterostructure compounds. Previously, a topological superconductor has been predominantly conceived to result from a topologically nontrivial band subject to an intrinsic or external superconducting proximity effect. Here, we propose a new class of topological superconductors that are uniquely induced by unconventional pairing. They exhibit a boundary-obstructed higher-order topological character and, depending on their dimensionality, feature unprecedentedly robust Majorana bound states or hinge modes protected by chiral symmetry. We predict the 112 family of iron pnictides, such as  $\text{Ca}_{1-x}\text{La}_x\text{FeAs}_2$ , to be highly suited material candidates for our proposal, which can be tested by edge spectroscopy. Because of the boundary obstruction, the topologically nontrivial feature of the 112 pnictides does not reveal itself for a bulk-only torus band analysis without boundaries, and as such, it had evaded previous investigations. Our proposal not only opens a new arena for highly stable Majorana modes in high-temperature superconductors but also provides the smoking gun for extended  $s$ -wave order in the iron pnictides.

DOI: [10.1103/PhysRevX.10.041014](https://doi.org/10.1103/PhysRevX.10.041014)Subject Areas: Condensed Matter Physics,  
Strongly Correlated Materials,  
Superconductivity

Iron-based high-temperature (high- $T_c$ ) superconductors have recently appeared as an exciting platform to realize topological superconductivity at high temperatures [1–9]. Because of an intrinsic superconducting proximity effect, the surfaces in these materials can host Majorana zero modes (MZMs), evidence of which has been observed in the vortex core of  $\text{Fe}(\text{Te},\text{Se})$  and  $(\text{Li}_{1-x}\text{Fe}_x)\text{OHFeSe}$  crystals [10–14]. In other words, a band inversion between the Fe  $d$  and the ligand  $p$  orbitals is found, which then culminates with the superconducting proximity imposed by the particle-particle instability at the Fermi level. While this band inversion appears to be rather generic for the

pnictides, current experimental evidence suggests that the topological superconducting phase necessitates significant tuning of Fermi-level and chemical composition.

In unconventional high- $T_c$  superconductors, the pairing symmetry is as essential, as it can be difficult to directly identify it. In cuprates, only several years after their discovery, a  $d$ -wave pairing symmetry was unambiguously proven by detecting the  $\pi$  phase shift in corner-junction interferometer experiments [15]. In iron-based superconductors, the pairing symmetry has been the subject of a long-lasting debate ever since their discovery a decade ago. An  $s_{\pm}$ -wave pairing, possessing a sign-reversed gap on hole and electron pockets in momentum space, has been proposed for iron-based superconductors with some indirect evidence in neutron scattering and scanning tunneling microscopy [16–22]. So far, however, no decisive experiment has been proposed to distinguish an  $s_{\pm}$ -wave from a sign-unchanged  $s$ -wave pairing because both states share the same  $A_{1g}$  symmetry character. The  $s_{\pm}$ -wave pairing was suggested to realize DIII topological superconductors [23]. As we will show in this work,  $s_{\pm}$  waves and  $s$  waves,

\*xianxinwu@gmail.com

†cx156@psu.edu

‡jphu@iphy.ac.cn

Published by the American Physical Society under the terms of the [Creative Commons Attribution 4.0 International license](https://creativecommons.org/licenses/by/4.0/). Further distribution of this work must maintain attribution to the author(s) and the published article's title, journal citation, and DOI.

despite their identical symmetry character, can give rise to different topological phases, and thus, we claim that the topological aspects in iron-based high- $T_c$  superconductors can shine a light on this outstanding problem [23].

Higher-order topological phases [24–29] are a new family of phases of matter with the defining property of hosting fractional charges or topological states at corners or hinges of the material. In 2D insulators, these phases manifest fractional corner charges protected by crystalline symmetries and are directly related to the positions of the Wannier centers of the occupied bands [28] or to the topology of its Wannier bands [26,27]. In superconductors, despite the absence of a Wannier description, particle-hole and/or chiral symmetries can also protect the existence of corner-localized MZMs. Recently, several proposals have been put forward for the realization of higher-order topological superconductors (HOTSC) in 2D or 3D [25,30–44], some of which include certain iron-based superconductor compounds [30,31,39,43,44]. Setting aside the fact that the complete characterization of HOTSC by topological invariants is still missing, there is, in addition, a significant disconnect between the toy models studied in those works and actual material candidates.

In order to understand the new class of superconductors we propose in this work, we develop a novel fused perspective on the current fields of unconventional superconductivity and higher-order topological states of matter. Specifically, we show that  $s_{\pm}$ -wave symmetry pairing, together with the topological properties in the 112 family of iron pnictides, drives the material into a HOTSC that hosts a Kramers pair of MZMs at each corner of each unit layer. Different from previous proposals, the MZMs are particularly robust, as they do not depend on crystal symmetries but are protected by chiral symmetry. The demonstration of high-order topology in this family of compounds will provide the “smoking gun” for  $s_{\pm}$ -wave pairing. Remarkably, the topological phase we find for this material has the property of being adiabatically connected to the trivial phase in the absence of boundaries, but, once boundaries are introduced, an edge-localized obstruction topologically separates it from the trivial phase. This property, referred to as boundary topological obstruction, was originally identified in the minimal model for a higher-order topological insulator hosting a quantized quadrupole moment protected by reflection symmetries [26,27]. In insulators, boundary topological obstructions have recently been explained in terms of the Wannier centers of the occupied bands [45]. Here, we generalize the concept of boundary topological obstructions to superconductors—for which a Wannier description is absent—and identify the 112 family of iron pnictides as the first intrinsic material realization of boundary-obstructed HOTSC. The existence of MZMs in boundary-obstructed HOTSCs is a clear signature of its nontrivial topology. Upon a phase transition into a trivial phase, the bulk remains gapped; only the edges

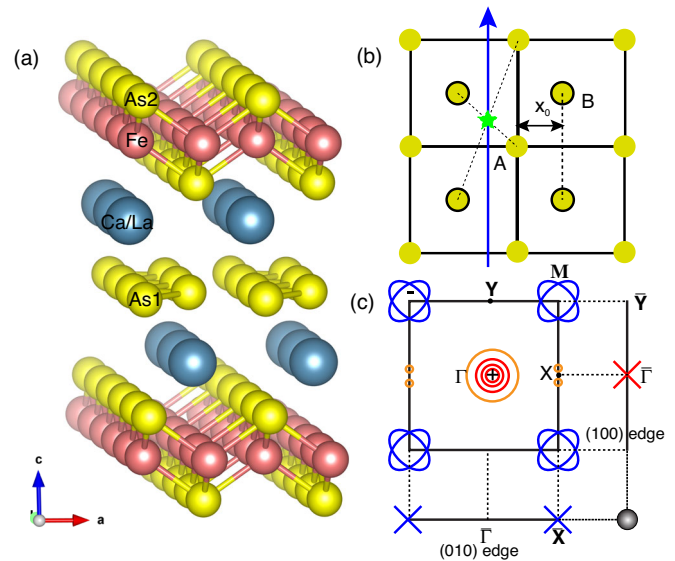


FIG. 1. Crystal structure and Fermi surfaces for  $(\text{Ca}, \text{La})\text{FeAs}_2$ . (a) Crystal structure for  $(\text{Ca}, \text{La})\text{FeAs}_2$ . (b) Lattice model for the As1 layers, where As1 atoms form a zigzag chain along  $y$ . (c) Fermi surfaces and pairing gap functions for  $(\text{Ca}, \text{La})\text{FeAs}_2$ . The red and blue curves represent the Fermi surfaces from FeAs layers in the presence of  $s_{\pm}$  pairing. The superconducting gaps possess a sign change between hole pockets around  $\Gamma$  and electron pockets around  $\mathbf{M}$ . The orange curves are Fermi surfaces from As1 layers. The edge Dirac cone from As1 layers acquires a positive (negative) superconducting gap for the (100) edge [(010) edge] in proximity to the bulk hole (electron) pockets around  $\Gamma$  ( $\mathbf{M}$ ). There is a Majorana Kramers pair (gray circles) at each corner where two edges meet.

become gapless, providing one-dimensional channels for the MZMs to hybridize as they disappear into the trivial phase.

The detection of MZMs in this material would be decisive evidence for  $s_{\pm}$ -wave pairing in iron-based superconductors for the following reason: The 112 family of iron pnictides, including  $\text{Ca}_{1-x}\text{La}_x\text{FeAs}_2$  [46] and  $(\text{Ca}, \text{Pr})\text{FeAs}_2$  [47], with  $T_c$  up to 47 K [48], are intrinsic topological insulator-high  $T_c$  superconductor heterostructures [49,50], with a staggered intercalation between zigzag, chainlike, As1 layers with the quantum spin Hall state and the superconducting Fe-As layers along the  $c$  axis, as shown in Fig. 1(a). The edge Dirac cones from the As1 layers at two orthogonal (100) and (010) edges are in proximity to projections of bulk pockets around  $\Gamma$  and  $\mathbf{M}$  from adjacent FeAs layers, respectively. The  $s_{\pm}$ -wave pairing with opposite gap functions on pockets around  $\Gamma$  and  $\mathbf{M}$  points will create the Majorana Kramers pairs at corners, as demonstrated in Fig. 1(c).

In what follows, we first investigate  $s_{\pm}$  pairing in  $\text{Ca}_{1-x}\text{La}_x\text{FeAs}_2$  and relate the bulk spectrum to that of its edges, which gives rise to the mechanism that realizes the corner MZMs. We then demonstrate that under  $s_{\pm}$  pairing, the topological phase in this material is boundary obstructed by showing that across the topological phase

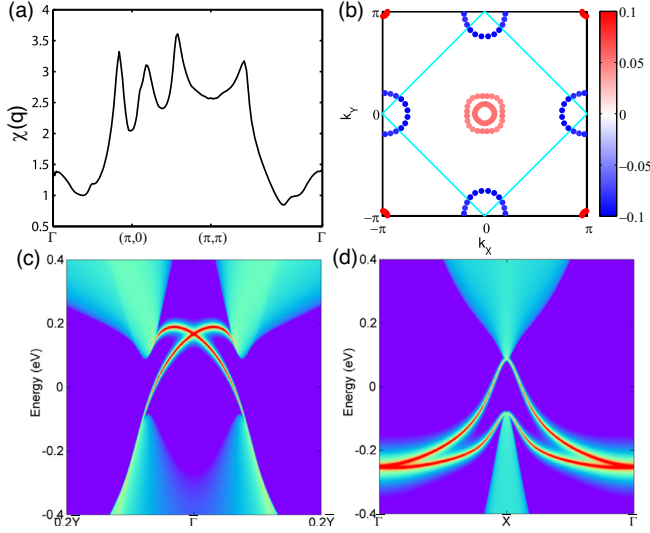


FIG. 2. Spin susceptibility and  $s_{\pm}$ -wave gap function for  $\text{CaFeAs}_2$  and edge states for As1 layers. (a) Distribution of the largest eigenvalues for RPA spin susceptibility matrices. (b) Dominant  $s_{\pm}$ -wave state from RPA calculations in one-Fe Brillouin zone. The interaction parameters are  $U = 1.4$  eV and  $J/U = 0.1$  with Kanamori relations  $U = U' + 2J$  and  $J = J'$ . The blue lines represent the Brillouin zone for a two-Fe unit cell. Edge states for As1 layers in  $\text{CaFeAs}_2$ : (c) (100) edge, (d) (010) edge.

transition (TPT) between the topological and trivial phases, the energy gap only closes at the boundary of a slab configuration, while it remains open in the bulk. Finally, since the two phases are protected by chiral symmetry, we propose a new quantity, the edge winding number, as the invariant that captures the corresponding topological obstruction, and we show that this invariant jumps by an integer across a TPT.

$s_{\pm}$  pairing in  $\text{Ca}_{1-x}\text{La}_x\text{FeAs}_2$ .—We take  $\text{CaFeAs}_2$  as a typical example of the 112-type. Besides the hole pockets around  $\Gamma$  and electron pockets around  $\mathbf{M}$  from FeAs layers, there are additional Fermi surfaces in  $\text{CaFeAs}_2$  attributed to the zigzag As1 layers [Fig. 1(c)]. As the correlation effect is relatively weak in As atoms, the pairing state of  $\text{CaFeAs}_2$  is expected to be dominantly determined by the Fermi surfaces from FeAs layers. Here, we adopt a five-band model whose band structure fits well with those in DFT calculations [see Sec. I in the Supplemental Material (SM) [51]]. Figure 2(a) displays the spin susceptibility. The peak around  $(\pi, 0)$  is attributed to the Fermi surface nesting between the hole and electron pockets. Consequently, the dominant pairing is  $s_{\pm}$ -wave type from the effective repulsive electron-electron interactions mediated by spin fluctuations [16,52]. Figure 2(b) shows the typical gap function of  $s_{\pm}$  pairing from random phase approximation (RPA) calculations for  $\text{CaFeAs}_2$ , revealing a sign change in superconducting gaps between hole and electron pockets (see Sec. II in the SM [51]). The sign

change and gap size can also be well described by a simple form factor  $\cos k_x \times \cos k_y$  in one-Fe unit cell originating from the next-nearest neighbor antiferromagnetic exchange coupling [53]. Unlike the  $d$ -wave state in cuprates, in which a sign change occurs in orthogonal directions,  $s_{\pm}$  pairing with a sign change in momentum space is extremely difficult to be detected via Josephson interferometry. Although some evidence for the existence of sign change in pairing states has been provided in inelastic neutron scattering and scanning tunneling microscopy measurements [16–22], a decisive signature for  $s_{\pm}$  pairing is still missing in iron pnictides. In the following, we show that  $s_{\pm}$  pairing gives rise to a HOTSC phase in  $\text{CaFeAs}_2$  with Majorana corner states, which can be regarded as direct evidence for  $s_{\pm}$  pairing.

*Effective model for As1 layers.*—We start with the tight-binding model for the As1 layers. A two-dimensional four-band model on a square lattice [Fig. 1(b)] has been derived to capture the band structure attributed to  $p_x$  and  $p_y$  orbitals of two As1 atoms in one unit cell. We introduce the operator  $\psi_{\mathbf{k}\sigma}^{\dagger} = [c_{Ax\sigma}^{\dagger}(\mathbf{k}), c_{Ay\sigma}^{\dagger}(\mathbf{k}), c_{Bx\sigma}^{\dagger}(\mathbf{k}), c_{By\sigma}^{\dagger}(\mathbf{k})]$ , where  $c_{\alpha\eta\sigma}^{\dagger}(\mathbf{k})$  is a fermionic creation operator, with  $\sigma, \eta$ , and  $\alpha$  being spin, orbital, and sublattice indices, respectively. The tight-binding Hamiltonian reads

$$\mathcal{H}_0 = \sum_{\mathbf{k}\sigma} \psi_{\mathbf{k}\sigma}^{\dagger} h(\mathbf{k}) \psi_{\mathbf{k}\sigma}. \quad (1)$$

The matrix elements in the Hamiltonian  $h(\mathbf{k})$  are provided in Sec. III in the SM [51]. A band inversion occurs at the  $\mathbf{X}$  point, and it generates two gapless Dirac cones in the bulk dispersion along the  $\mathbf{X}$ - $\mathbf{M}$  path without spin-orbit coupling (SOC), protected by the screw axis along  $y$  [49,50]. Two small pockets appear around the  $\mathbf{X}$  point derived from these cones, demonstrated by orange circles in Fig. 1(c) and supported by ARPES experiments [54–56]. Furthermore, including SOC opens a gap in the Dirac cones, and the As1 layers become  $\mathbb{Z}_2$  topologically nontrivial, leading to an intrinsic topological insulator-high  $T_c$  superconductor heterostructure in  $\text{CaFeAs}_2$ . Around the  $\mathbf{X}$  point, the bulk dispersion of As1 layers can be described by an effective Hamiltonian  $\mathcal{H}_{\text{eff}}^{\mathbf{X}} = \sum_{\mathbf{k}} \tilde{\psi}_{\mathbf{k}}^{\dagger} h_{\text{eff}}(\mathbf{k}) \tilde{\psi}_{\mathbf{k}}$  with basis  $\tilde{\psi}_{\mathbf{k}}^{\dagger} = (c_{Xk,-\uparrow}^{\dagger}, c_{Xk,+\uparrow}^{\dagger}, c_{Xk,-\downarrow}^{\dagger}, c_{Xk,+\downarrow}^{\dagger})$ , where “+/-” denotes the eigenvalue of  $C_{2z}$  for eigenstates at the  $\mathbf{X}$  point, and

$$h_{\text{eff}}(\mathbf{k}) = \epsilon_0(\mathbf{k}) + M(\mathbf{k})\sigma_z - A_1 k_x s_0 \sigma_2 + A_2 k_y s_3 \sigma_1. \quad (2)$$

Here,  $\epsilon_0(\mathbf{k}) = C_0 + C_1 k_x^2 + C_2 k_y^2$  and  $M(k) = M_0 - B_1 k_x^2 - B_2 k_y^2$ , and  $\sigma$  and  $s$  are Pauli matrices in orbital and spin degrees of freedom. The parameters in the model are given in Sec. IV of the SM [51]. The edge states can be obtained by solving a semi-infinite system along the  $x$  or  $y$  direction within the tight-binding model. For the (100) edge, a distorted Dirac cone appears around the  $\bar{\Gamma}$  point located above the Fermi level, as shown in Fig. 2(c), while, for the

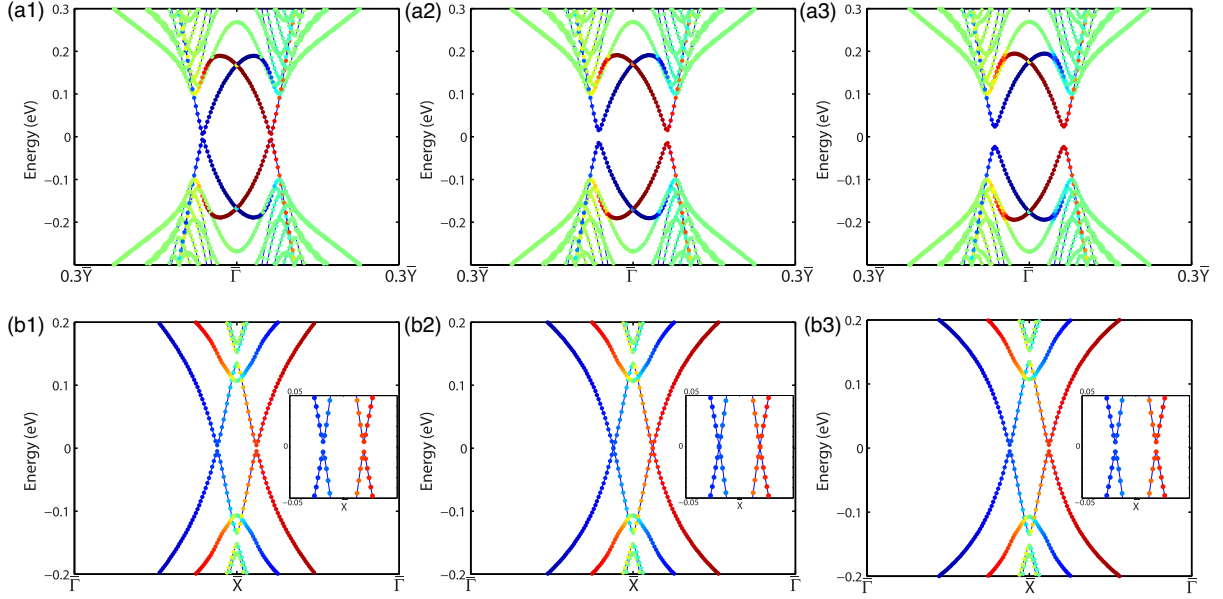


FIG. 3. Evolution of band structures for the (100) edge (a) and the (010) edge (b) as a function of the  $s_{\pm}$  pairing  $\Delta_1$ . The plots in each column are generated with the same parameters, and the adopted parameters in three columns (from left to right) are  $\Delta_1 = 0$ ,  $\Delta_1 = 51$  meV, and  $\Delta_1 = 100$  meV, with a fixed  $\Delta_0 = 5$  meV. The color code shows the average position of each state. The blue and red circles denote the left (top) and right (bottom) localized edge states at the (100) [(010)] edges, respectively. The green circles represent extended bulk states.

(010) edge, a Dirac cone occurs around the  $\bar{X}$  point and is embedded in the bulk conduction bands, as shown in Fig. 2(d). We emphasize that the Fermi level for both edges only crosses the lower part of the edge Dirac cone within a relatively large electron doping region from the substitution of La/Pr for Ca in experiments.

Below  $T_c$ , the As1 layers become superconducting through the proximity effect to the adjacent FeAs layers. We model the superconducting pairing on As1 layers the same way as in FeAs layers and consider a spin-singlet intra-orbital pairing within the same sublattice. The corresponding pairing Hamiltonian reads

$$\mathcal{H}_{\text{SC}} = \sum_{a\nu\sigma k} \sigma [\Delta_0 + 2\Delta_1(\cos k_x + \cos k_y)] \times c_{a\nu\sigma}^{\dagger}(\mathbf{k})c_{a\nu\bar{\sigma}}^{\dagger}(-\mathbf{k}) + \text{H.c.}, \quad (3)$$

where  $\Delta_0$  and  $\Delta_1$  are the on-site pairing and pairing between the next-nearest-neighbor sites, respectively. The  $\Delta_1$  term gives rise to the well-known  $s_{\pm}$ -wave pairing in iron-based superconductors. Owing to the absence of spin-flip SOC terms, the Bogoliubov–de Gennes (BdG) tight-binding Hamiltonian  $\mathcal{H}_{\text{BdG}} = \mathcal{H}_0 + \mathcal{H}_{\text{SC}}$  can be written as two block diagonal parts  $\mathcal{H}_{\text{BdG}}^{\uparrow\downarrow}$  and  $\mathcal{H}_{\text{BdG}}^{\downarrow\uparrow}$  (see Sec. V in the SM [51]). In each block, time-reversal and particle-hole symmetries are absent, but chiral symmetry is preserved; thus, each block belongs to class AIII in the tenfold classification.

*Boundary-obstruction and phase transitions.*—To study the edge properties of the As1 layers, we consider a slab configuration for the above BdG Hamiltonian  $\mathcal{H}_{\text{BdG}}^{\uparrow\downarrow}$  with an

open boundary along either the  $x$  or  $y$  direction. With the on-site pairing term  $\Delta_0$ , the edge states from As1 layers open a gap, as shown in Figs. 3(a1) and 3(b1). Now, we investigate the effect of  $s_{\pm}$ -wave pairing on these edge states. At the (100) edge, the gap of edge states around  $\bar{\Gamma}$  monotonously increases with increasing  $\Delta_1$ , as shown in Figs. 3(a1) to 3(a3). For the (010) edge, however, the gap around  $\bar{X}$  exhibits a rather different behavior. Upon  $\Delta_1$  increasing to 0.051 eV, the gap closes, and a pair of gapless modes with linear dispersion appears [Fig. 3 (b2)]. Further increasing  $\Delta_1$  reopens the gap, suggesting a TPT that separates a  $\Delta_0$ -dominated phase from a  $\Delta_1$ -dominated phase. Note that throughout this transition, there is no gap closing in the bulk states (see Sec. VIII in the SM [51]). In fact, we show in Sec. VII of the SM [51] that all the symmetry-indicator invariants due to the  $C_{2z}$  and reflection symmetries in the lattice structure of  $\mathcal{H}_{\text{BdG}}$  identically vanish due to time-reversal symmetry, which is a necessary condition for the existence of boundary-obstructed phases.

To calculate the effective pairing at the edges, we first analytically obtain the wave functions of the edge states by solving  $\mathcal{H}_{\text{eff}}$  with open boundary conditions and then projecting the bulk pairing on the edge states [30,57]. The obtained pairings at the Dirac points on the (100) and (010) edges are

$$\Delta_{\text{eff}}^{(100)} = \Delta_0 + 2\Delta_1 \frac{M_0}{B_1}, \quad (4)$$

$$\Delta_{\text{eff}}^{(010)} = \Delta_0 - 2\Delta_1 \frac{M_0}{B_2}. \quad (5)$$

We find that  $\Delta_0$  provides the same pairing at the two edges while the  $s_{\pm}$ -wave pairing  $\Delta_1$  provides an opposite pairing sign. This case can be heuristically understood from Fig. 1(c). The edge Dirac states appear around  $\bar{\Gamma}$  and  $\bar{X}$  for the (100) and (010) edges; the momentum-independent term proportional to  $\Delta_0$  induces the same positive superconducting gap at both edges; the  $s_{\pm}$ -wave pairing, on the other hand, induces superconducting gaps with opposite signs as the corresponding Dirac cones are in proximity to the bulk superconducting gap around  $\Gamma$  and  $M$  at the (100) and (010) edges, respectively [see Fig. 1(c)]. At a fixed nonzero value of  $\Delta_0$ , with increasing  $\Delta_1$ ,  $\Delta_{\text{eff}}^{(100)}$  monotonously increases while  $\Delta_{\text{eff}}^{(010)}$  first decreases to zero, followed by an increase in amplitude albeit with opposite sign, which is consistent with the aforementioned numerical calculations. The finite chemical potential at the edges with respect to Dirac points should be taken into consideration, but their relatively small values have a negligible effect on the effective pairing (see Sec. VI in the SM [51]).

To characterize the topological nature of the TPT, let us focus on the blocks  $\mathcal{H}_{\text{BdG}}^{\uparrow\downarrow}$  and  $\mathcal{H}_{\text{BdG}}^{\downarrow\uparrow}$ , each of which belongs to class AIII. Hamiltonians in this class are topologically characterized by the 1D winding number [58], defined by

$$\nu_1 = \frac{i}{2\pi} \int_{\text{BZ}} dk \text{Tr}[q_k^{-1} \partial_k q_k].$$

Here, the unitary  $q_k$  matrix is the off-diagonal part of the so-called  $Q$  matrix, given by

$$Q_k = \mathbf{1} - 2P_k = \begin{pmatrix} 0 & q_k \\ q_k^\dagger & 0 \end{pmatrix}$$

within the eigenbasis of chiral symmetry, where  $P_k$  is the projection operator of the Hamiltonian for a slab model  $\mathcal{H}_{\text{BdG,slab}}^{\uparrow\downarrow}$  with  $N$  lattice sites. We first consider the winding number on a slab configuration with an open boundary along the (010) direction. The total winding number  $\nu_1$  is zero across the TPT (see Sec. VIII in the SM [51]). Motivated by the fact that the bands close at the (010) edges of the slab during the TPT, we define a site-resolved winding number by projecting the total winding number  $\nu_1$  into the lattice site basis as

$$\nu_1^i = \frac{i}{2\pi} \sum_{\gamma} \int_{\text{BZ}} dk [q_k^{-1} \partial_k q_k]_{i\gamma, i\gamma}, \quad (6)$$

such that  $\nu_1 = \sum_{i=1}^N \nu_1^i$ . Here,  $i$  is the index for the lattice site and  $\gamma$  denotes the sublattice or orbital index (details are given in Sec. VIII in the SM [51]). This site-resolved winding number resembles the site-resolved polarization defined in Ref. [27] to calculate the edge-localized dipole moments in insulators, including the boundary-obstructed quadrupole topological insulator [26]. The dependence of  $\nu_1^i$  on the site  $i$  for the HOTSC and trivial phases is

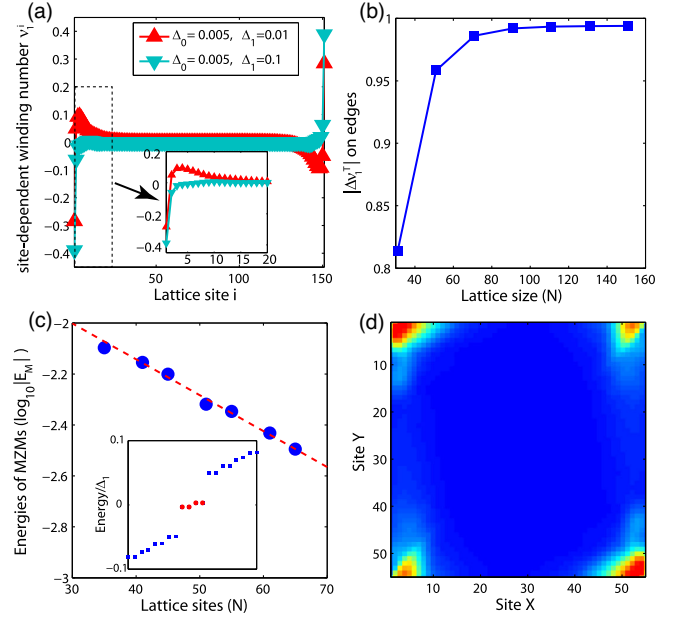


FIG. 4. Edge winding number and energy and spatial pattern for MZMs. (a) Site-resolved winding numbers for the (010) edge with  $N = 150$  unit cells along  $y$  in the two topologically distinct phases. (b) Winding number difference  $\Delta\nu_1^T$  as a function of the lattice size  $N$ . (c) Energy of the MZMs as a function of the lattice size for a square geometry. The inset shows typical energy spectra for the full lattice. (d) Probability density functions of the MZMs for a square geometry with eight MZMs (each corner hosts a Kramers pair of MZM) with  $65 \times 65$  lattice sites.

displayed by the blue and red curves in Fig. 4(a). For both curves, one can see that the contribution to the winding number mainly comes from edges, with the opposite edges having opposite contributions. We also notice that the profile of  $\nu_1^i$  near one edge [see the zoom-in, Fig. 4(a)] has a substantial difference between the HOTSC and trivial phases. We define the edge winding numbers  $\nu_1^T$  and  $\nu_1^B$  for the top and bottom edges, respectively, by summing  $\nu_1^i$  for the upper-half part ( $i = 1, \dots, N/2$ ) and lower-half part ( $i = N/2 + 1, \dots, N$ ) of the slab and examine the winding number change  $|\Delta\nu_1^{T/B}|$  between two phases for the upper- and lower-half parts as a function of the lattice size  $N$ . As shown in Fig. 4(b), we find that the winding number change  $|\Delta\nu_1^T|$  approaches 1 in the thermodynamic limit ( $N \rightarrow \infty$ ). Thus, the edge winding number  $\nu_1^{T/B}$  characterizes the different topologies across the TPT in our new class of superconductors.

*Majorana corner states.*—In the  $\Delta_1$ -dominated phase, the (100) and (010) edges have opposite superconducting gaps, belonging to topologically distinct phases. As a consequence, MZMs are expected to occur at the corners where they meet. We adopt the Hamiltonian  $\mathcal{H}_{\text{BdG}}$ , with both open boundary conditions along the  $x$  and  $y$  directions, and performed calculations with several lattice sizes. There are eight midgap states, and their energies are zero up

to finite-size effects. We examine the energy splitting due to the hybridization of the MZMs at different corners by plotting the energies  $E_M$  of midgap states as a function of lattice size in Fig. 4(c). The linear relationship between  $\log_{10}(E_m)$  and lattice size suggests that  $E_M$  goes to zero in the thermodynamic limit, which is compatible with the existence of zero-energy states exponentially localized at the corners of the lattice, as shown in Fig. 4(d). At each corner, there are two zero-energy states forming a Majorana Kramers pair. The appearance of MZMs at the corners supports our prediction of a HOTSC phase with boundary obstruction in  $\text{CaFeAs}_2$ .

*Discussion.*—As the 112 family of iron pnictides is 3D and the interlayer coupling is relatively weak, the helical Majorana states, localized at the hinges between (100) and (010) surfaces, have a weak dispersion along  $k_z$ . MZMs can also appear at corners or hinges between nonorthogonal surfaces, as long as the corresponding surface states have the opposite effective superconducting gap in proximity to the bulk  $s_{\pm}$  pairing. Therefore, the  $s_{\pm}$  pairing is directly manifested by the appearance of MZMs at hinges, protected by chiral symmetry and irrespective of crystalline symmetries. We contrast our proposal with that of Ref. [23]. There, a heterostructure couples Rashba semiconductors with nodeless iron-based superconductors. Unlike our proposal, the realization of such a structure would require a large Rashba SOC. It is also worth noting that the toy model in Ref. [31] realizes a bulk- and boundary-obstructed HOTSC with and without the fourfold rotational symmetry, respectively. The 112 family of iron pnictides, to some extent, can be considered as a realization of the toy model in Ref. [31] with boundary-obstructed HOTSC. The MZMs we find are robust against impurities and disorders in real material scenarios that always break crystalline symmetries. In realistic materials, the symmetries are reduced compared with the adopted model. Under this scenario, SOC terms could, in principle, appear that flip the spin sectors; however, the Majorana Kramers pairs will survive as they are protected by time-reversal symmetry. The detection of corner or hinge MZMs in  $\text{CaFeAs}_2$  hence provides the smoking gun for the  $s_{\pm}$  pairing in iron pnictides. As the Fermi level only crosses the lower part of edge Dirac cones in As1 layers within a wide electron-doping range, the MZMs can survive in electron-doped compounds  $\text{Ca}_{1-x}\text{La}_x\text{FeAs}_2$ , providing a new high-temperature platform for MZMs without fine-tuning.

In particular, because of the weak interlayer coupling in the 112 family of iron pnictides, the cleavage occurs between Ca/La layers and As1 layers or FeAs layers, generating step edges on (001) surfaces. At the ends of the step edges, which can be viewed as corners of As1 layers, MZMs can give rise to a zero-bias peak in the scanning tunneling microscopy measurements (see Sec. VIII in the SM [51]), and their localized nature can be manifested in spatial zero-energy mapping [see Fig. 4(d)]. Hinge MZMs

are expected to induce a zero-bias anomaly in transport measurements with junctions in contact with the corresponding hinge [59]. The Majorana Kramers pair can split under an in-plane magnetic field. As the Sb doping can enhance both  $T_c$  and the quantum spin Hall gap of the As1 layer [48],  $\text{Ca}_{1-x}\text{La}_x\text{Fe}(\text{As}_{1-y}\text{Sb}_y)_2$  can be a good choice for samples in experimental measurements.

*Conclusion.*—We propose the 112 family of iron pnictides as the first material realization of boundary-obstructed topological superconductivity, owing to their intrinsic  $s_{\pm}$  pairing and effective topological insulator-high  $T_c$  superconductor heterostructure profile. The edge topological obstruction, independent of crystalline symmetries and uniquely characterized by the edge winding number, provides a robust platform for the realization of MZMs, which *en passant* also constitutes decisive evidence for  $s_{\pm}$ -wave pairing in the 112 pnictides.

We thank J. Yu and N. Hao for helpful discussions. W. A. B. acknowledges support from the Eberly Postdoctoral Fellowship at the Pennsylvania State University. C. X. L. acknowledges the support of the Office of Naval Research (Grant No. N00014-18-1-2793), DOE Grant No. DE-SC0019064, and the Kaufman New Initiative research Grant No. KA2018-98553 of the Pittsburgh Foundation. J. H. is supported by the Ministry of Science and Technology of China 973 program (Grant No. 2017YFA0303100), National Science Foundation of China (Grant No. NSFC-11888101), and the Strategic Priority Research Program of CAS (Grant No. XDB28000000). The work in Würzburg is funded by the Deutsche Forschungsgemeinschaft (DFG, German Research Foundation) through Project-ID 258499086—SFB 1170 and through the Würzburg-Dresden Cluster of Excellence on Complexity and Topology in Quantum Matter—*ct.qmat* Project-ID 39085490—EXC 2147.

- 
- [1] N. Hao and J. Hu, *Topological Phases in the Single-Layer FeSe*, *Phys. Rev. X* **4**, 031053 (2014).
  - [2] X. Wu, S. Qin, Y. Liang, H. Fan, and J. Hu, *Topological Characters in  $\text{Fe}(\text{Te}_{1-x}\text{Se}_x)$  Thin Films*, *Phys. Rev. B* **93**, 115129 (2016).
  - [3] Z. Wang, P. Zhang, G. Xu, L. K. Zeng, H. Miao, X. Xu, T. Qian, H. Weng, P. Richard, A. V. Fedorov, H. Ding, X. Dai, and Z. Fang, *Topological Nature of the  $\text{FeSe}_{0.5}\text{Te}_{0.5}$  Superconductor*, *Phys. Rev. B* **92**, 115119 (2015).
  - [4] G. Xu, B. Lian, P. Tang, X.-L. Qi, and S.-C. Zhang, *Topological Superconductivity on the Surface of Fe-Based Superconductors*, *Phys. Rev. Lett.* **117**, 047001 (2016).
  - [5] P. Zhang, K. Yaji, T. Hashimoto, Y. Ota, T. Kondo, K. Okazaki, Z. Wang, J. Wen, G. D. Gu, H. Ding, and S. Shin, *Observation of Topological Superconductivity on the Surface of an Iron-Based Superconductor*, *Science* **360**, 182 (2018).

- [6] P. Zhang *et al.*, *Multiple Topological States in Iron-Based Superconductors*, *Nat. Phys.* **15**, 41 (2019).
- [7] X. Shi, Z.-Q. Han, P. Richard, X.-X. Wu, X.-L. Peng, T. Qian, S.-C. Wang, J.-P. Hu, Yu.-J. Sun, and H. Ding, *FeTe<sub>1-x</sub>Se<sub>x</sub> Monolayer Films: Towards the Realization of High-Temperature Connate Topological Superconductivity*, *Sci. Bull.* **62**, 503 (2017).
- [8] X. L. Peng, Y. Li, X. X. Wu, H. B. Deng, X. Shi, W. H. Fan, M. Li, Y. B. Huang, T. Qian, P. Richard, J. P. Hu, S. H. Pan, H. Q. Mao, Y. J. Sun, and H. Ding, *Observation of Topological Transition in High- $T_c$  Superconducting Monolayer FeTe<sub>1-x</sub>Se<sub>x</sub> Films on SrTiO<sub>3</sub>(001)*, *Phys. Rev. B* **100**, 155134 (2019).
- [9] N. Hao and J. Hu, *Topological Quantum States of Matter in Iron-Based Superconductors: From Concept to Material Realization*, *Natl. Sci. Rev.* **6**, 213 (2018).
- [10] J. X. Yin, Z. Wu, J. H. Wang, Z. Y. Ye, J. Gong, X. Y. Hou, L. Shan, A. Li, X. J. Liang, X. X. Wu, J. Li, C. S. Ting, Z. Q. Wang, J. P. Hu, P. H. Hor, H. Ding, and S. H. Pan, *Observation of a Robust Zero-Energy Bound State in Iron-Based Superconductor Fe(Te,Se)*, *Nat. Phys.* **11**, 543 (2015).
- [11] D. Wang, L. Kong, P. Fan, H. Chen, S. Zhu, W. Liu, L. Cao, Y. Sun, S. Du, J. Schneeloch, R. Zhong, G. Gu, L. Fu, H. Ding, and H.-J. Gao, *Evidence for Majorana Bound States in an Iron-Based Superconductor*, *Science* **362**, 333 (2018).
- [12] Q. Liu, C. Chen, T. Zhang, R. Peng, Y.-J. Yan, C.-H.-P. Wen, X. Lou, Yu.-L. Huang, J.-P. Tian, X.-L. Dong, G.-W. Wang, W.-C. Bao, Q.-H. Wang, Z.-P. Yin, Z.-X. Zhao, and D.-L. Feng, *Robust and Clean Majorana Zero Mode in the Vortex Core of High-Temperature Superconductor (Li<sub>0.84</sub>Fe<sub>0.16</sub>)OHFeSe*, *Phys. Rev. X* **8**, 041056 (2018).
- [13] L. Kong, S. Zhu, M. Papaj, H. Chen, L. Cao, H. Isobe, Y. Xing, W. Liu, D. Wang, P. Fan, Y. Sun, S. Du, J. Schneeloch, R. Zhong, G. Gu, L. Fu, H.-J. Gao, and H. Ding, *Half-Integer Level Shift of Vortex Bound States in an Iron-Based Superconductor*, *Nat. Phys.* **15**, 1181 (2019).
- [14] T. Machida, Y. Sun, S. Pyon, S. Takeda, Y. Kohsaka, T. Hanaguri, T. Sasagawa, and T. Tamegai, *Zero-Energy Vortex Bound State in the Superconducting Topological Surface State of Fe(Se,Te)*, *Nat. Mater.* **18**, 811 (2019).
- [15] D. J. Van Harlingen, *Phase-Sensitive Tests of the Symmetry of the Pairing State in the High-Temperature Superconductors—Evidence for  $d_{x^2-y^2}$  Symmetry*, *Rev. Mod. Phys.* **67**, 515 (1995).
- [16] P. J. Hirschfeld, M. M. Korshunov, and I. I. Mazin, *Gap Symmetry and Structure of Fe-Based Superconductors*, *Rep. Prog. Phys.* **74**, 124508 (2011).
- [17] A. D. Christianson, E. A. Goremychkin, R. Osborn, S. Rosenkranz, M. D. Lumsden, C. D. Malliakas, I. S. Todorov, H. Claus, D. Y. Chung, M. G. Kanatzidis, R. I. Bewley, and T. Guidi, *Unconventional Superconductivity in Ba<sub>0.6</sub>K<sub>0.4</sub>Fe<sub>2</sub>As<sub>2</sub> from Inelastic Neutron Scattering*, *Nature (London)* **456**, 930 (2008).
- [18] M. D. Lumsden, A. D. Christianson, D. Parshall, M. B. Stone, S. E. Nagler, G. J. MacDougall, H. A. Mook, K. Lokshin, T. Egami, D. L. Abernathy, E. A. Goremychkin, R. Osborn, M. A. McGuire, A. S. Sefat, R. Jin, B. C. Sales, and D. Mandrus, *Two-Dimensional Resonant Magnetic Excitation in BaFe<sub>1.84</sub>Co<sub>0.16</sub>As<sub>2</sub>*, *Phys. Rev. Lett.* **102**, 107005 (2009).
- [19] A. D. Christianson, M. D. Lumsden, S. E. Nagler, G. J. MacDougall, M. A. McGuire, A. S. Sefat, R. Jin, B. C. Sales, and D. Mandrus, *Static and Dynamic Magnetism in Underdoped Superconductor BaFe<sub>1.92</sub>Co<sub>0.08</sub>As<sub>2</sub>*, *Phys. Rev. Lett.* **103**, 087002 (2009).
- [20] Y. Qiu, W. Bao, Y. Zhao, C. Broholm, V. Stanev, Z. Tesanovic, Y. C. Gasparovic, S. Chang, J. Hu, B. Qian, M. Fang, and Z. Mao, *Spin Gap and Resonance at the Nesting Wave Vector in Superconducting FeSe<sub>0.4</sub>Te<sub>0.6</sub>*, *Phys. Rev. Lett.* **103**, 067008 (2009).
- [21] T. Hanaguri, S. Niitaka, K. Kuroki, and H. Takagi, *Unconventional  $s$ -Wave Superconductivity in Fe(Se,Te)*, *Science* **328**, 474 (2010).
- [22] S. Grothe, S. Chi, P. Dosanjh, R. Liang, W. N. Hardy, S. A. Burke, D. A. Bonn, and Y. Pennec, *Bound States of Defects in Superconducting LiFeAs Studied by Scanning Tunneling Spectroscopy*, *Phys. Rev. B* **86**, 174503 (2012).
- [23] F. Zhang, C. L. Kane, and E. J. Mele, *Time-Reversal-Invariant Topological Superconductivity and Majorana Kramers Pairs*, *Phys. Rev. Lett.* **111**, 056402 (2013).
- [24] F. Zhang, C. L. Kane, and E. J. Mele, *Surface State Magnetization and Chiral Edge States on Topological Insulators*, *Phys. Rev. Lett.* **110**, 046404 (2013).
- [25] W. A. Benalcazar, J. C. Y. Teo, and T. L. Hughes, *Classification of Two-Dimensional Topological Crystalline Superconductors and Majorana Bound States at Disclinations*, *Phys. Rev. B* **89**, 224503 (2014).
- [26] W. A. Benalcazar, B. A. Bernevig, and T. L. Hughes, *Quantized Electric Multipole Insulators*, *Science* **357**, 61 (2017).
- [27] W. A. Benalcazar, B. A. Bernevig, and T. L. Hughes, *Electric Multipole Moments, Topological Multipole Moment Pumping, and Chiral Hinge States in Crystalline Insulators*, *Phys. Rev. B* **96**, 245115 (2017).
- [28] Z. Song, Z. Fang, and C. Fang, *( $d - 2$ )-Dimensional Edge States of Rotation Symmetry Protected Topological States*, *Phys. Rev. Lett.* **119**, 246402 (2017).
- [29] J. Langbehn, Y. Peng, L. Trifunovic, F. von Oppen, and P. W. Brouwer, *Reflection-Symmetric Second-Order Topological Insulators and Superconductors*, *Phys. Rev. Lett.* **119**, 246401 (2017).
- [30] Z. Yan, F. Song, and Z. Wang, *Majorana Corner Modes in a High-Temperature Platform*, *Phys. Rev. Lett.* **121**, 096803 (2018).
- [31] Q. Wang, C.-C. Liu, Y.-M. Lu, and F. Zhang, *High-Temperature Majorana Corner States*, *Phys. Rev. Lett.* **121**, 186801 (2018).
- [32] C.-H. Hsu, P. Stano, J. Klinovaja, and D. Loss, *Majorana Kramers Pairs in Higher-Order Topological Insulators*, *Phys. Rev. Lett.* **121**, 196801 (2018).
- [33] Y. Wang, M. Lin, and T. L. Hughes, *Weak-Pairing Higher Order Topological Superconductors*, *Phys. Rev. B* **98**, 165144 (2018).
- [34] X. Zhu, *Tunable Majorana Corner States in a Two-Dimensional Second-Order Topological Superconductor Induced by Magnetic Fields*, *Phys. Rev. B* **97**, 205134 (2018).
- [35] M. Geier, L. Trifunovic, M. Hoskam, and P. W. Brouwer, *Second-Order Topological Insulators and Superconductors*

- with an Order-Two Crystalline Symmetry, *Phys. Rev. B* **97**, 205135 (2018).
- [36] E. Khalaf, *Higher-Order Topological Insulators and Superconductors Protected by Inversion Symmetry*, *Phys. Rev. B* **97**, 205136 (2018).
- [37] X.-H. Pan, K.-J. Yang, L. Chen, G. Xu, C.-X. Liu, and X. Liu, *Lattice-Symmetry-Assisted Second-Order Topological Superconductors and Majorana Patterns*, *Phys. Rev. Lett.* **123**, 156801 (2019).
- [38] Z. Wu, Z. Yan, and W. Huang, *Higher-Order Topological Superconductivity: Possible Realization in Fermi Gases and  $\text{Sr}_2\text{RuO}_4$* , *Phys. Rev. B* **99**, 020508(R) (2019).
- [39] R.-X. Zhang, W. S. Cole, and S. D. Sarma, *Helical Hinge Majorana Modes in Iron-Based Superconductors*, *Phys. Rev. Lett.* **122**, 187001 (2019).
- [40] Y. Volpez, D. Loss, and J. Klinovaja, *Second-Order Topological Superconductivity in  $\pi$ -Junction Rashba Layers*, *Phys. Rev. Lett.* **122**, 126402 (2019).
- [41] S. A. A. Ghorashi, X. Hu, T. L. Hughes, and E. Rossi, *Second-Order Dirac Superconductors and Magnetic Field Induced Majorana Hinge Modes*, *Phys. Rev. B* **100**, 020509 (R) (2019).
- [42] Y.-J. Wu, J. Hou, Y.-M. Li, X.-W. Luo, X. Shi, and C. Zhang, *In-Plane Zeeman-Field-Induced Majorana Corner and Hinge Modes in an  $s$ -Wave Superconductor Heterostructure*, *Phys. Rev. Lett.* **124**, 227001 (2020).
- [43] R.-X. Zhang, W. S. Cole, X. Wu, and S. D. Sarma, *Higher-Order Topology and Nodal Topological Superconductivity in  $\text{Fe}(\text{Se},\text{Te})$  Heterostructures*, *Phys. Rev. Lett.* **123**, 167001 (2019).
- [44] X. Wu, X. Liu, R. Thomale, and C.-X. Liu, *High- $T_c$  Superconductor  $\text{Fe}(\text{Se},\text{Te})$  Monolayer: An Intrinsic, Scalable and Electrically-Tunable Majorana Platform*, [arXiv:1905.10648](https://arxiv.org/abs/1905.10648).
- [45] E. Khalaf, W. A. Benalcazar, T. L. Hughes, and R. Queiroz, *Boundary-Obstructed Topological Phases*, [arXiv:1908.00011](https://arxiv.org/abs/1908.00011).
- [46] N. Katayama, K. Kudo, S. Onari, T. Mizukami, K. Sugawara, Y. Sugiyama, Y. Kitahama, K. Iba, K. Fujimura, N. Nishimoto, M. Nohara, and H. Sawa, *Superconductivity in  $\text{Ca}_{1-x}\text{La}_x\text{FeAs}_2$ : A Novel 112-Type Iron Pnictide with Arsenic Zigzag Bonds*, *J. Phys. Soc. Jpn.* **82**, 123702 (2013).
- [47] H. Yakita, H. Ogino, T. Okada, A. Yamamoto, K. Kishio, T. Tohei, Y. Ikuhara, Y. Gotoh, H. Fujihisa, K. Kataoka, H. Eisaki, and J.-i. Shimoyama, *A New Layered Iron Arsenide Superconductor:  $(\text{Ca},\text{Pr})\text{FeAs}_2$* , *J. Am. Chem. Soc.* **136**, 846 (2014).
- [48] K. Kudo, Y. Kitahama, K. Fujimura, T. Mizukami, H. Ota, and M. Nohara, *Superconducting Transition Temperatures of up to 47 K from Simultaneous Rare-Earth Element and Antimony Doping of 112-Type  $\text{CaFeAs}_2$* , *J. Phys. Soc. Jpn.* **83**, 093705 (2014).
- [49] X. Wu, C. Le, Y. Liang, S. Qin, H. Fan, and J. Hu, *Effect of As-Chain Layers in  $\text{CaFeAs}_2$* , *Phys. Rev. B* **89**, 205102 (2014).
- [50] X. Wu, S. Qin, Y. Liang, C. Le, H. Fan, and J. Hu,  *$\text{CaFeAs}_2$ : A Staggered Intercalation of Quantum Spin Hall and High-Temperature Superconductivity*, *Phys. Rev. B* **91**, 081111(R) (2015).
- [51] See Supplemental Material at <http://link.aps.org/supplemental/10.1103/PhysRevX.10.041014> for detailed discussions.
- [52] R. Thomale, C. Platt, W. Hanke, and B. A. Bernevig, *Mechanism for Explaining Differences in the Order Parameters of  $\text{FeAs}$ -based and  $\text{FeP}$ -based pnictide superconductors*, *Phys. Rev. Lett.* **106**, 187003 (2011).
- [53] K. Seo, B. A. Bernevig, and J. Hu, *Pairing Symmetry in a Two-Orbital Exchange Coupling Model of Oxyapnictides*, *Phys. Rev. Lett.* **101**, 206404 (2008).
- [54] M. Y. Li, Z. T. Liu, W. Zhou, H. F. Yang, D. W. Shen, W. Li, J. Jiang, X. H. Niu, B. P. Xie, Y. Sun, C. C. Fan, Q. Yao, J. S. Liu, Z. X. Shi, and X. M. Xie, *Significant Contribution of  $4p$  Orbitals to the Low-Lying Electronic Structure of the 112-Type Iron-Based Superconductor  $\text{Ca}_{0.9}\text{La}_{0.1}\text{FeAs}_2$* , *Phys. Rev. B* **91**, 045112 (2015).
- [55] S. Jiang, C. Liu, H. Cao, T. Birol, J. M. Allred, W. Tian, L. Liu, K. Cho, M. J. Krogstad, J. Ma, K. M. Taddei, M. A. Tanatar, M. Hoesch, R. Prozorov, S. Rosenkranz, Y. J. Uemura, G. Kotliar, and N. Ni, *Structural and Magnetic Phase Transitions in  $\text{Ca}_{0.73}\text{La}_{0.27}\text{FeAs}_2$  with Electron-Overdoped  $\text{FeAs}$  Layers*, *Phys. Rev. B* **93**, 054522 (2016).
- [56] Z. T. Liu, X. Z. Xing, M. Y. Li, W. Zhou, Y. Sun, C. C. Fan, H. F. Yang, J. S. Liu, Q. Yao, W. Li, Z. X. Shi, D. W. Shen, and Z. Wang, *Observation of the Anisotropic Dirac Cone in the Band Dispersion of 112-Structured Iron-Based Superconductor  $\text{Ca}_{0.9}\text{La}_{0.1}\text{FeAs}_2$* , *Appl. Phys. Lett.* **109**, 042602 (2016).
- [57] S.-B. Zhang and B. Trauzettel, *Detection of Second-Order Topological Superconductors by Josephson Junctions*, *Phys. Rev. Research* **2**, 012018 (2020).
- [58] C.-K. Chiu, J. C. Y. Teo, A. P. Schnyder, and S. Ryu, *Classification of Topological Quantum Matter with Symmetries*, *Rev. Mod. Phys.* **88**, 035005 (2016).
- [59] M. J. Gray, J. Freudenstein, S. Y. F. Zhao, R. O'Connor, S. Jenkins, N. Kumar, M. Hoek, A. Kopec, S. Huh, T. Taniguchi, K. Watanabe, R. Zhong, C. Kim, G. D. Gu, and K. S. Burch, *Evidence for Helical Hinge Zero Modes in an  $\text{Fe}$ -Based Superconductor*, *Nano Lett.* **19**, 4890 (2019).